Electronic Supplementary Material (ESI) for Nanoscale.
This journal is © The Royal Society of Chemistry 2023

Supplementary Information to "Evaluating strain and doping of Janus MoSSe from phonon mode shifts supported by ab-initio DFT calculations"

Jennifer Schmeink, Vladislav Musytschuk, Erik Pollmann, Stephan Sleziona, André Maas, Peter Kratzer and Marika Schleberger*

Faculty of Physics and CENIDE, University of Duisburg-Essen, Duisburg, Germany

**E-mail: marika.schleberger@uni-due.de,*

Phone: +49 (0)203 379-1600

Abstract. Supplementary to the data shown in the main manuscript, we present topography images from atomic force microscopy measurements correlated with Raman mappings of the sample to ensure its homogeneity and monolayer status. Moreover, Raman spectra of a multilayer $MoSe_2$ part of a sample after the processing. This gives additional information on how the process cuts and replaces the Se-bonds and shows an as-processed heterostructure of a monolayer MoSSe on top of few-layer $MoSe_2$. Additional DFT calculations for the doping and stain levels of monolayer MoS_2 are shown for comparison of doping level of the Janus monolayer. Moreover, we present a more detailed comparison of the temperature-dependent PL of MoSSe in comparison with $MoSe_2$ and MoS_2, both of which show realistic values for the parameters of the respective Varshni-fits, corroborating our data for the Janus MoSSe monolayer further. Lastly, we present a calibration spectrum for the TCSPC measurement and explain some of its follies, as well as spectra of the other TCSPC measurements from different points on monolayer MoSSe.

1. AFM Topography Correlated with Raman Mappings

An important quality characteristic of the Janus monolayer after processing is its homogeneity which we will discuss in the following. We observe it via Raman-mappings in direct correlation to atomic force microscopy (AFM) images. The result is shown in Fig. S1 before and after the conversion. As seen in the topography (see Fig. S1 (a)), before the thermal sulfurization process, the as-exfoliated flake consists of a thicker part and a monolayer region. This is also reflected in the Raman mapping (b), which shows the typical shift of the A_{1g} out-of-plane vibrational mode to lower wave numbers when thinned down. The images taken before processing show residues from the glue of the tape used for the mechanical exfoliation as well as other adsorbates. These, however, do not appear to have any influence on the Raman signal in the mapping shown in Fig. S1 (b). After the thermal sulfurization process, we observe in the topography in Fig. S1 (c) that the flake appears to be significantly cleaner. The adsorbates and glue residues have desorbed after the annealing and therefore the surface of the flake appears much smoother. Additionally, the step height is reduced by ~ 300 pm from 1.5 nm to 1.2 nm for the same reason, while still being larger than the nominal monolayer height of 3.28 Å [1]. This height discrepancy can be attributed to both surface and trapped water layers. The trapped water underneath exfoliated flakes is encapsulated by the flake itself and therefore cannot be fully removed, even when annealed at high temperatures. Previous studies have shown that this leads to an increased step height in the AFM on the order of 1 nm [2], which is in good agreement with our step height discrepancy. The processing does of course not only affect the morphology but also the materials' composition, which is clearly shown by the Raman mapping presented in Fig. S1 (d). A very distinctive difference between the monolayer MoSSe and the thicker multilayer part can be seen. The zoom-in shows the homogeneity of the Janus monolayer as derived from the A_{1g} peak position. Correlating this mapping with the AFM image in (c), one can identify the few inhomogeneous spots in the monolayer as structural inhomogeneities. These particles could be sulfur residues from the processing, as it is known that

gaseous sulfur preferably forms clusters [3]. Important to note here: the mapping highlights only the most dominant mode (excluding the Si-peak), as the scale bar shows. Therefore, not shown in this mapping, is the fact that the multilayer region can be interpreted as a heterostructure, as the top-most layer is also converted to Janus MoSSe, while the layers below remain $MoSe_2$. For full spectra taken on multilayer heterostructure parts, see the supporting information, Fig. S2.

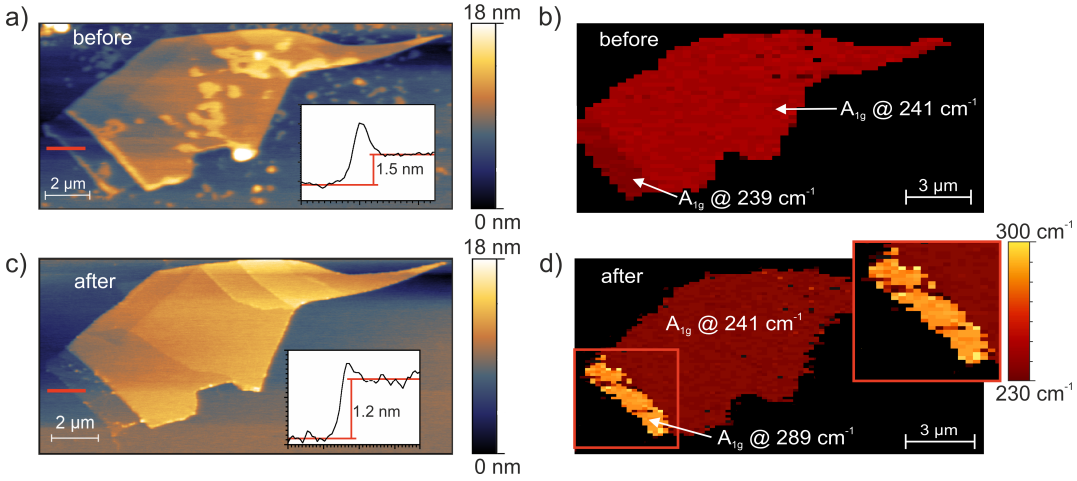

FIGURE S1. **Correlating ambient AFM topography and Raman mappings.** (a) AFM topography and (b) Raman mapping of the A_{1g}-mode before, and (c) and (d) after the thermal processing. The insets in the AFM images show the height profile of the monolayer at the red lines in the images. The mapping after the process shows the homogeneity in the monolayer as highlighted in the zoom-in shown in (d).

2. MULTILAYER $MoSe_2$ POST PROCESSING

As alluded to in the main body of this scientific paper, our method of sulfurizing as-exfoliated $MoSe_2$ flakes does not only yield high quality Janus MoSSe monolayer, but also multilayered heterostructures. Such a multilayered flake before and after the sulfurization process is seen in Fig. S2 (a). Note that the layer numbers in the image inset is acquired through AFM data. Here, the Raman signature of the multilayer acquired shows clearly the shift from pure $MoSe_2$ to a mixture of such with MoSSe typical modes emerging as well. The shear modes S of the $MoSe_2$ multilayer are preserved in the heterostructure,

although its intensity drops, as there is one layer less to contribute plus the top most layer MoSSe shields the $MoSe_2$ layers underneath. Moreover, we clearly see a shift of the A_{1g} mode of the $MoSe_2$ to lower wavenumbers, while the Defect peak D shifts slightly to higher wavenumbers. This can be attributed to a higher Defect density in the $MoSe_2$, especially a Se-vacancy increase [4]. This can be expected as the thermal etching process targets the Se-atoms specifically and thus this observation is to be expected. Almost of the same intensity as the $MoSe_2$ A_{1g} peak is the out-of-plane vibrational mode of the Janus MoSSe monolayer. The position of the latter is at its monolayer position of 289 cm^{-1} (see Fig. S2 (b)), indicating that indeed only the topmost layer seems to be exchanging Se- with S-atoms during the processing. Fig. S2 (b) insinuates that the monolayer MoSSe A_{1g} modes intensity is significantly less than that of the heterostructure, however, it is important to understand, that these spectra are calibrated to the Si-peak and its intensity increases naturally when observing a thinner material ontop. Meaning, the seen decrease in intensity is only due to the increase of the Si-signal as the obscuring power of the monolayer is less than that of a multilayered material.

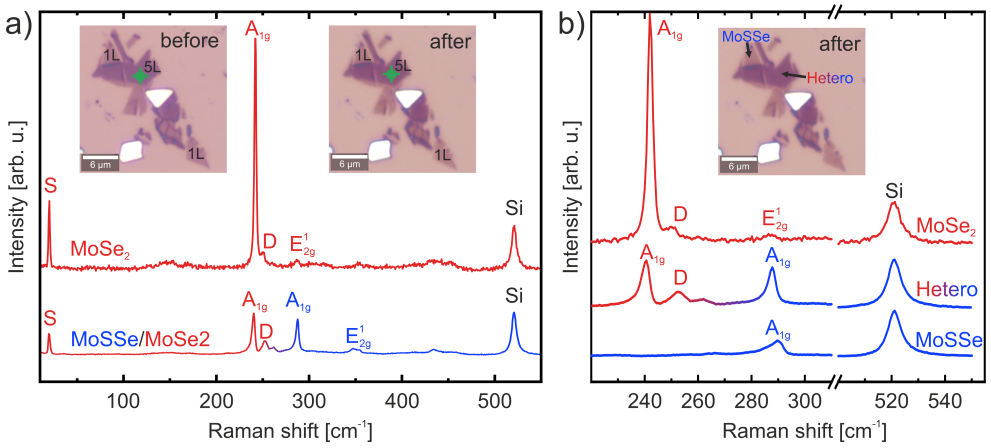

FIGURE S2. **$MoSSe/MoSe_2$ heterostructure.** (a) Raman spectra before and after the sulfurization process on a multi layer part of an as-exfoliated flake taken at the green dot in the images. S indicates a shear mode typical for $MoSe_2$ bulk, D denotes the Se-vacancy dependent defect peak of $MoSe_2$. In (b) is a smaller section of the spectra shown, as well as a spectrum taken at the monolayer after the process. The spectra are all normalized on the Si-peak in order to compare intensities before and after.

3. Stain and doping of MoS_2 as reference

As indicated in the main body of this manuscript the doping of the fabricated Janus structure seems comparable to that of our as exfoliated monolayer MoS_2, therefore determining an approximate level of doping of the MoS_2 reference can lead to a more conclusive comparison. The level of relative doping and strain can be calculated from the relative mode positions of MoS_2, as shown by Pollmann et al. [5]. The there proposed matrix is given as

$$\begin{pmatrix} \Delta Strain \\ \Delta Doping \end{pmatrix} = \begin{pmatrix} -0.490\ \%\ /\ \mathrm{cm}^{-1} & 0.073\ \%\ /\ \mathrm{cm}^{-1} \\ 0.088 \cdot 10^{13}\ \mathrm{cm}^{-2}/\mathrm{cm}^{-1} & -0.464 \cdot 10^{13}\ \mathrm{cm}^{-2}/\mathrm{cm}^{-1} \end{pmatrix} \cdot \begin{pmatrix} \Delta E^1_{2g} \\ \Delta A_{1g} \end{pmatrix},$$

with ΔE^1_{2g} and ΔA_{1g} being the difference in mode position to the reference sample. A representative Raman spectrum of our exfoliated MoS_2 monolayers is given in Fig. S3. The spectrum is normalized onto the Si-peak position of 520.6 cm^{-1} [6]. From this spectrum the mode position is determined to be 385.3 cm^{-1} and 403.3 cm^{-1} for the in- and out-of-plane vibrational mode, respectively. As a reference we rely on the measurements of exfoliated MoS_2 on a sapphire substrate of Panasci et al., who report monolayers with a compressive strain of $\varepsilon_{ref} = -0.25$ % and a n-type doping level of $n_{ref} = -0.5 \cdot 10^{13}$ cm^{-2}* for E^1_{2g} and A_{1g} Raman modes at 386.191 cm^{-1} and 405.346 cm^{-1}, respectively [7]. With these values as the reference we can deduce the relative doping and strain of our exfoliated samples. We conclude our MoS_2 are more tense by $\Delta Strain = 0.396$ % and more n-doped by $\Delta Doping = -0.334 \cdot 10^{13}$ cm^{-2} in comparison to the reference. With the given doping n_{ref} and strain ε_{ref} we can thus conclude our MoS_2 monolayer to have a tensile strain level of $\varepsilon = 0.146$ % and an intrinsic n-type doping of roughly $n = -0.834 \cdot 10^{13}$ cm^{-2}. These values seem appropriate for the context of as-exfoliated monolayer MoS_2 on SiO_2 substrates. For an overview of the values see Tab. S1. As aforementioned a similar, if not even larger level

* Note: Due to the reverse sign of the reference doping compared to our definition, we saw fit to change it accordingly.

of doping is expected for the Janus MoSSe monolayer, as deduced from the similar intensity of the trion contribution in the photoluminescence spectra.

TABLE S1. Raman modes and the calculated strain and doping of the monolayer MoS_2.

	$\omega_{E^1_{2g}}$ [cm^{-1}]	$\omega_{A_{1g}}$ [cm^{-1}]	$\Delta\omega$ [cm^{-1}]	ε [%]	n [$\cdot 10^{13}$ cm^{-2}]
ML MoS_2	385.3 ± 0.2	403.3 ± 0.2	18.0 ± 0.3	0.146 ± 0.026	-0.834 ∓ 0.034

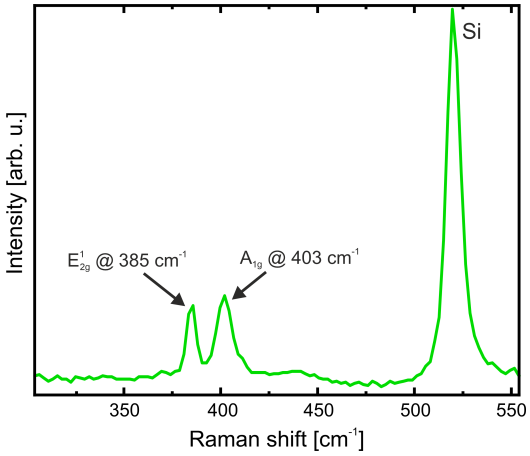

FIGURE S3. **Raman spectrum of as exfoliated monolayer MoS_2 at room temperature.** The spectrum is normalized onto the Si-peak. Labeled are the two Raman active modes of MoS_2 E^1_{2g} and A_{1g}.

4. Temperature dependent PL in Mo-based TMDCs

Additionally to the temperature dependent measurement for the Janus monolayer MoSSe, we show here the ones corresponding to the monolayers of the two base TMDCs. Fig. S4 shows the PL spectra, as well as the corresponding Varshni-fits for both A- and B-excitons. From these plots we deduce the 0 K transition energies for the two excitons as: 1.610 eV, 1.758 eV, and 1.845 eV for the A-exciton and 1.814 eV, 1.938 eV, and 2.006 eV of monolayer $MoSe_2$, MoSSe, and MoS_2, respectively. Moreover, we obtain values for the material specific parameters α and $\beta \approx \Theta_{Debye}$. These are for $MoSe_2$ $\alpha = 2.52 \cdot 10^{-4}$ eV/K and $\Theta_{Debye} \approx$ 19.513 K, or $\alpha = 1.48 \cdot 10^{-4}$ eV/K and $\Theta_{Debye} \approx 43.303$ K for its A-, and B-exciton's fits, respectively. For MoS_2 these come out to be $\alpha = 2.18 \cdot 10^{-4}$ eV/K and $\Theta_{Debye} \approx$

453.10 K, or $\alpha = 2.28 \cdot 10^{-4}$ eV/K and $\Theta_{Debye} \approx 151.22$ K for its A-, and B-exciton's fits, respectively. These results are for both materials in good agreement with previous publications [8,9] and theoretical predictions [10]. An overview of these data is given in Table S2.

TABLE S2. Summary of the fit parameters obtained from the different materials' excitons, through applying the Varshni equation. E_0 denotes the 0 K transition energy, α and β are material specific constants.

Monolayer	$MoSe_2$		MoSSe		MoS_2	
Exciton	A	B	A	B	A	B
E_0 [eV]	1.610	1.814	1.758	1.938	1.845	2.006
α [10^{-4} eV/K]	2.52	1.48	3.78	3.94	2.18	2.28
β [K]	19.513	43.303	214.05	230.05	453.10	151.22

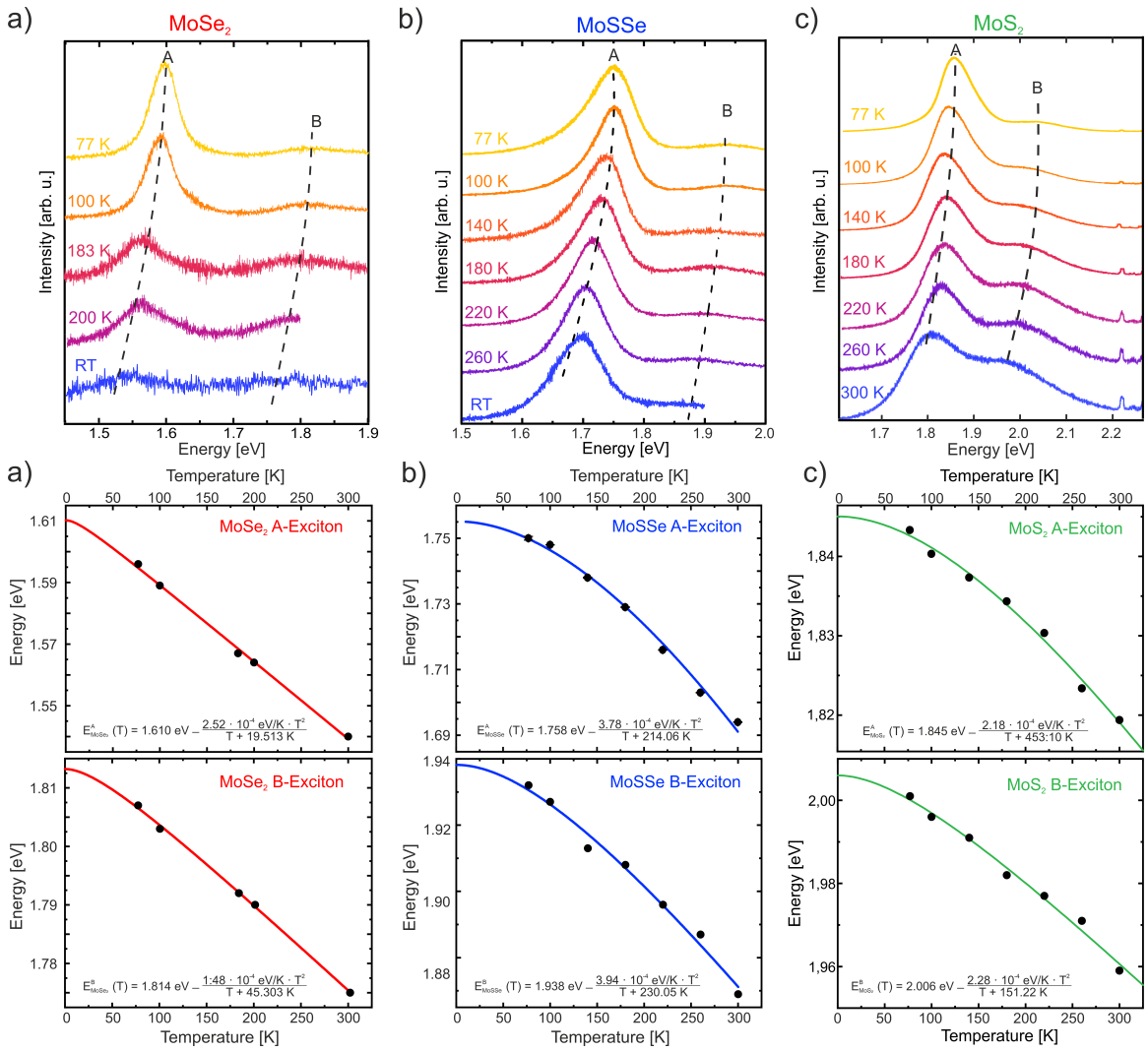

FIGURE S4. **Temperature dependence of the normalized photoluminescence spectra of different TMDCs.** (a) $MoSe_2$, (b) MoSSe and (c) $MoSe_2$. Together with their corresponding Varshni fits for both their A- and B-excitons. Continuing the trend to 0 K gives rise to E_0 for each exciton in each material, this being for the A-excitons 1.610 eV, 1.758 eV, and 1.845 eV and for the B-excitons 1.814 eV, 1.938 eV, and 2.006 eV, respectively.

5. COMPUTATIONAL DATA

To clarify our conclusion for the theoretical evaluation of strain and doping in our Janus monolayer, we show in Fig. S5 the strain dependent curves for the Raman shift of the A_{1g}-

and E^1_{2g}-modes at the fixed doping level which we concluded to be the two possibilities for our sample. These are either a n-type doping of -0.57 $\cdot 10^{13}$ cm^{-2} or -1.18 $\cdot 10^{13}$ cm^{-2}. From the image one can see clearly that at these doping levels, the two modes can only occur with the measured Raman shifts of 289 cm^{-1} and 352 cm^{-1} at a single strain value each. Those are -0.8% and $+0.4\%$ for the weaker and the stronger n-type doping, respectively.

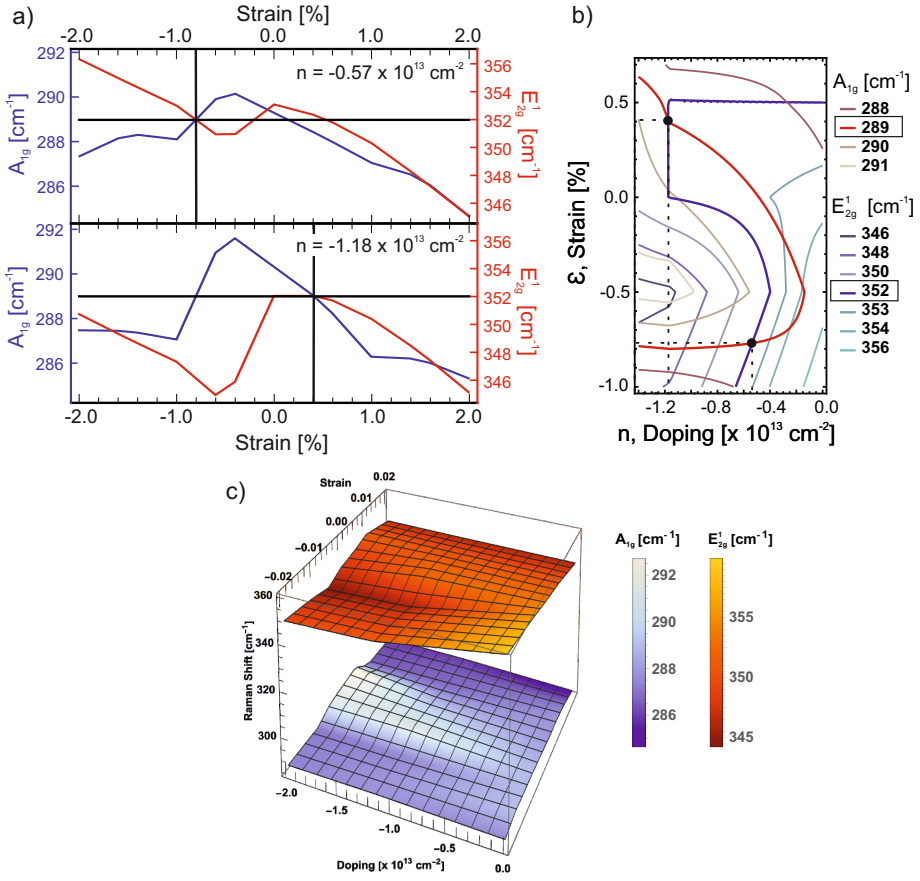

FIGURE S5. **Strain dependent Raman-mode shift for a constant doping level.** The (a) Raman shift dependence of the A_{1g}- (blue, left ordinate) and E^1_{2g}-mode (red, right ordinate) with variable strain. On top for a constant n-type doping of $-0.57 \cdot 10^{13}$ cm^{-2} and below for $-1.18 \cdot 10^{13}$ cm^{-2}. The horizontal line indicate the measured Raman shifts for the two modes. The two curves cross the horizontal line at the same abscissa at -0.8% and $+0.4\%$, respectively. (b) Different depiction of the same data, with a strain versus doping display and the A_{1g} and E^1_{2g} Raman modes as contour lines. This version shows the same strain-doping combinations at the points where the lines for the 289 cm^{-1} and 352 cm^{-1} lines cross. (c) Displays the two mode shifts in a three dimensional plot.

6. TCSPC data of monolayer MoSSe

As briefly mentioned in the main body of this publication, we calibrated the TCSPC measurement by aquiring a dark residue photon counting measurement. Such a calibration spectra is shown in Fig. S6. This serves as a representative for all calibrations done. As can be seen in the figure, the calibration shows the expected noise like spectra for the dark residue photon counting, however, a peak at 9 ns can be seen. This peak is not seen at all in uncalibrated TCSPC measurements of the MoSSe monolayer, therefore when calibrating our measurements, a divot in the data appears around the 9 ns mark. This is a setup error, therefore not a real feature of the MoSSe TCSPC measurement and thus we decided to omit the few points for the fit of the biexponential curve, as it would otherwise falsify our results.

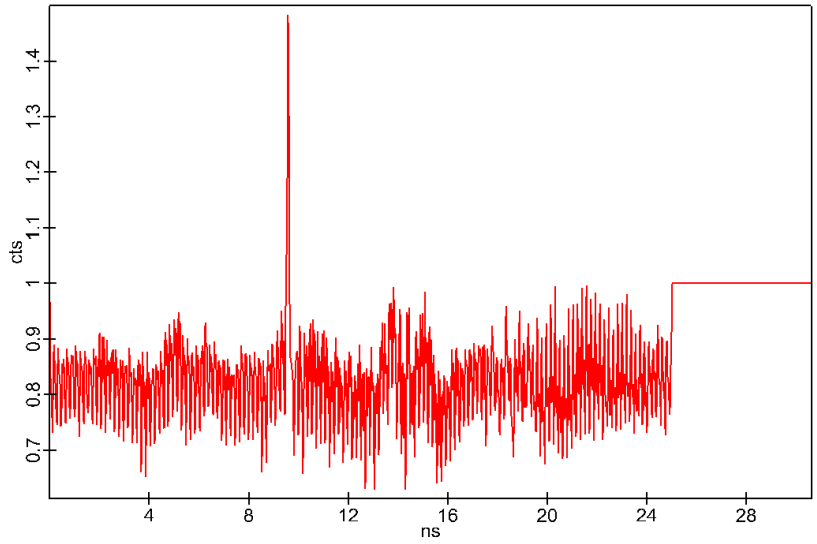

Figure S6. **Representative calibration spectrum for the TCSPC measurements.** Note a peak in the spectrum at 9 ns. This cannot be seen in the raw data of the TCSPC spectra, therefore this peak results in an over correction of the data, which can be seen as a divot in the calibrated spectra. Therefore, these few points can be excluded from the evaluation, as they do not represent a real phenomena.

The calibrated TCSPC measurements used to make a small statistic over different locations on the monolayer MoSSe is shown in Fig. S7. Note the different levels of signal-to-noise ratio, as the laser spot was sometimes a little bit more on the substrate and sometimes more on the multilayer part. Unfortunately, as the monolayer size was limited, we could not produce more accuracy. Nonetheless, all these decay show the typical longer and shorter lifetime, which we've been talking about in the main text, just the fit accuracy was somewhat limited for some of these measurements. A comprehensive overlook for the fit parameters of the TCSPC measurements and the calculated total average lifetime τ_{tot} is given in Tab. S3.

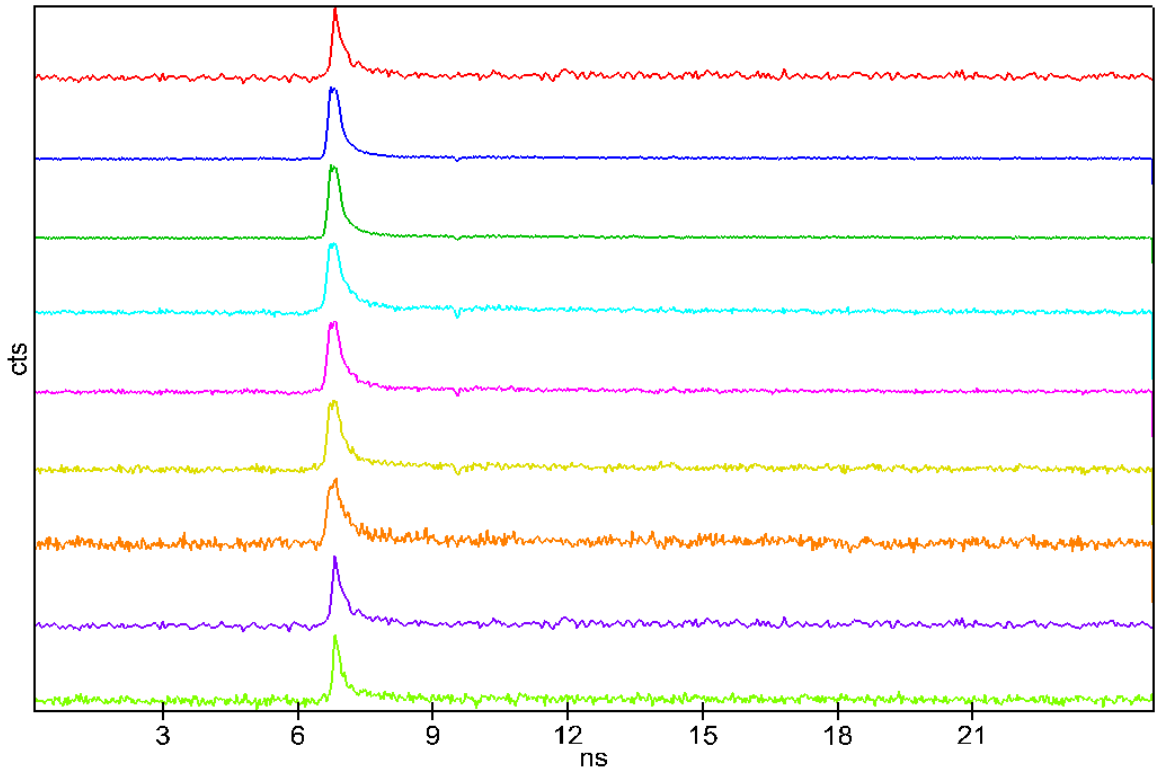

FIGURE S7. **TCSPC statistics.** All TCSPC calibrated spectra unaltered, as they were used to fit the biexponential decay function to. For the fits results see Tab. S3.

TABLE S3. Comprehensive overview of parameters obtained from fitting a biexponential decay function to the different TCSPC measurements seen in Fig. S7. τ_i are the lifetimes and $\Delta\tau_i$ the fits' error margin. The Amplitudes A_i are normalized to the total amplitude $A_{ges} = \sum_i A_i$ in order to better compare the fraction of each exponential decay to the total fit. The total average lifetime is calculated as described in the main body of this work. The average and its standard deviation of each parameter are given in the last two columns.

									Average	Std. dev.
τ_1 [ps]	122	193	253	185	219	213	124	120	179	48
$\Delta\tau_1$ [ps]	14	23	23	61	6	86	5	5		
A_1 / A_{ges}	0.863	0.829	0.877	0.848	0.921	0.843	0.784	0.766	0.841	0.046
τ_2 [ns]	1.01	1.232	4.748	2.72	3.97	2.88	0.76	0.69	2.251	1.460
$\Delta\tau_2$ [ns]	0.303	0.347	1.63	2.05	0.522	2.80	0.054	0.048		
A_2 / A_{ges}	0.137	0.171	0.123	0.152	0.079	0.157	0.216	0.234	0.159	0.046
τ_{tot} [ns]	0.627	0.783	3.513	2.024	2.507	2.120	0.523	0.483	1.573	1.058

References

[1] Cheng, Y. C., Zhu, Z. Y., Tahir, M. & Schwingenschlögl, U. Spin-orbit–induced spin splittings in polar transition metal dichalcogenide monolayers. EPL **102**, 57001 (2013).

[2] Ochedowski, O., Bussmann, B. K. & Schleberger, M. Graphene on mica - intercalated water trapped for life. Sci. Rep. **4**, 6003 (2014).

[3] Raghavachari, K., Rohlfing, C. M. & Binkley, J. S. Structures and stabilities of sulfur clusters. J. Chem. Phys. **93**, 5862–5874 (1990).

[4] Mahjouri-Samani, M. et al. Tailoring Vacancies Far Beyond Intrinsic Levels Changes the Carrier Type and Optical Response in Monolayer $MoSe_2$-x Crystals. Nano Letters **16**, 5213–5220 (2016).

[5] Pollmann, E. et al. Apparent differences between single layer molybdenum disulphide fabricated via chemical vapour deposition and exfoliation. Nanotechnology **31**, 505604 (2020).

[6] Ajito, K., Sukamto, J. P. H., Nagahara, L. A., Hashimoto, K. & Fujishima, A. Strain imaging analysis of Si using Raman microscopy. Journal of Vacuum Science & Technology A: Vacuum, Surfaces, and Films **13**, 1234–1238 (1995).

[7] Panasci, S. E. et al. Strain, Doping, and Electronic Transport of Large Area Monolayer MoS_2 Exfoliated on Gold and Transferred to an Insulating Substrate. ACS applied materials & interfaces **13**, 31248–31259 (2021).

[8] Korn, T., Heydrich, S., Hirmer, M., Schmutzler, J. & Schüller, C. Low-temperature photocarrier dynamics in monolayer MoS_2. Applied Physics Letters **99**, 102109 (2011).

[9] Lundt, N. et al. Monolayered $MoSe_2$: a candidate for room temperature polaritonics. 2D Materials **4**, 015006 (2017).

[10] Peng, B. et al. Thermal conductivity of monolayer MoS_2, $MoSe_2$, and WS_2: interplay of mass effect, interatomic bonding and anharmonicity. RSC Advances **6**, 5767–5773 (2016).